

# Thermodynamics and Kinetics of Solution Combustion Synthesis: $\text{Ni}(\text{NO}_3)_2$ + Fuels Systems

Narine Amirkhanyan<sup>1</sup>, Suren Kharatyan<sup>1,2</sup>, Khachatur Manukyan<sup>3\*</sup>, Ani Aprahamian<sup>3</sup>

<sup>1</sup> *Laboratory of Kinetics of SHS Processes, Institute of Chemical Physics NAS of Armenia, Yerevan 0014, Armenia*

<sup>2</sup> *Department of Chemistry, Yerevan State University, Yerevan 0025, Armenia*

<sup>3</sup> *Nuclear Science Laboratory, Department of Physics, University of Notre Dame, Notre Dame, Indiana 46556, United States*

\*Email: [kmanukya@nd.edu](mailto:kmanukya@nd.edu)

## Abstract

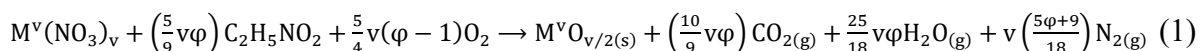
Solution combustion synthesis (SCS) utilizes exothermic self-propagating reactions to prepare nanoscale materials that can be used widely in energy, electronics, and biomedical technologies and other applications. SCS is a specific variety of a more general combustion synthesis (CS) method. Investigations of the thermodynamics, kinetics, and the mechanisms of SCS reactions, are not as well studied as the other CS processes. This work reports on a systematic study of the thermodynamics and kinetics of SCS reactions involving  $\text{Ni}(\text{NO}_3)_2$ , an oxidizer, and either glycine ( $\text{C}_2\text{H}_5\text{NO}_2$ ) or hexamethylenetetramine (HMT,  $\text{C}_6\text{H}_{12}\text{N}_4$ ) as fuels. A thermodynamic modeling approach, based on the Gibbs free energy minimization principle, is applied to the simultaneous calculations of the adiabatic temperatures and compositions of the equilibrium products. Our calculations reveal the influence of fuel-to-oxidizer ratio, amount of water, and the oxygen in air on the combustion temperature under adiabatic conditions and the composition of the resulting products. We have, in turn, measured the combustion temperature and phase composition of products and compared them with the calculations. Variations of drying times for the solutions yield precursor gels with varying water contents. This approach enables the manipulation of combustion parameters and confirms the use of calculated activation energies for reactions using the Merzhanov-Khaikin method. The results show that SCS reactions in fuel-lean solutions producing  $\text{NiO}$  have higher activation energy in contrast to reactions with fuel-rich solutions that form  $\text{Ni}$ . Reduction of activation energies due to the increase in the fuel-to-oxidizer ratio could be related to the observed change of the rate-limiting stages of the endothermic decomposition of the individual reactants to the exothermic decomposition of coordinate compounds formed between the reactants.

**Keywords:** solution combustion synthesis; equilibrium thermodynamics, kinetics, activation energy; reaction mechanism; nanoscale metal powders.

## 1. Introduction

Solution combustion synthesis (SCS) allows for the rapid preparation of nanoscale materials in bulk or thin-film forms [1]. This method employs exothermic self-propagating reactions in reactive solutions or gels for the preparation of nanoscale oxides [2–5], sulfides [6,7], nitrides [8], metals, and alloys [9,10] for the use of energy conversion and storage technologies [11–14], electronics [15,16], as well as environmental [17–20] and biomedical [21,22] applications. SCS is a specific variety of a more general combustion synthesis (CS) method, also known as self-propagating high-temperature synthesis (SHS) [23–27].

The reactants in these processes are metal nitrates (oxidizers) and organic compounds (fuels) [28,29]. The fuel should have a relatively low decomposition temperature (<600K) and high solubility in water. Some fuels can form complexes with metal ions, thus increasing the solubility of the reactants in the solvent. The molecular-level mixing of the multiple metal nitrates ensures the preparation of complex oxides with high uniformity for the constituents. An example of the SCS process is the reaction between a metal nitrate and glycine ( $\text{C}_2\text{H}_5\text{NO}_2$ ):



where  $v$  is the oxidation degree of the metal, and the  $\varphi$  is the fuel-to-oxidizer ratio. In the  $\varphi = 1$  (stoichiometric ratio), the nitrate supplies the oxygen required for complete combustion of the fuel, whereas the  $\varphi < 1$  or  $\varphi > 1$  represent fuel-lean or fuel-rich systems, respectively.

The duration of the SCS process is in the order of minutes, and the maximum temperature could be as high as 2000 K [30,31]. The solid products of the SCS reactions exhibit a porous morphology due to the release of a large volume of gases [32]. The microstructures of the materials depend on the characteristics of the liquid before the reaction initiation [1]. In most cases, the products consist of isotropic near-spherical, polyhedral, or irregular-shaped nanoscale crystalline grains of 10-100 nm.

A limitation of the SCS method is the relatively low level of control over the morphological uniformity of the products due to the complex nature of the process and the lack of sufficient knowledge on phase formation mechanisms. The kinetics and its relations to mechanisms of SCS reactions are not as thoroughly studied as other CS processes. The generally accepted understanding is that the microstructures of the materials depend on the reaction rate, the combustion temperatures, and the rates of gas release in the reactions. However, only a limited number of previous measurements report on the combustion temperature and wave propagation velocity. Adiabatic combustion temperature ( $T_{ad}$ ) calculations often substitute direct temperature measurements [33–42]. These calculations utilize *apriori* assumptions about the compositions of the products. The shortcoming of this approach is that the equilibrium products for a specific system is unknown and largely depend on the reaction temperatures.

A few studies have been reported on the kinetics of SCS reactions in order to establish the rate constants and rate laws for the successful scale-up of the processes [43]. Kumar et al. applied [9] the Kissinger model [44] to differential scanning calorimetry (DSC) data for the fuel-rich *nickel nitrate – glycine* system for the determination of the apparent activation energy. These authors suggest that the process consists of two stages. They assume that during the first stage, the decomposition of nickel nitrate and glycine release  $HNO_3$  and  $NH_3$ , respectively. The exothermic reaction between these species has an activation energy of  $\sim 125$  kJ/mol. The second stage is then attributed to the hydrogen reduction of  $NiO$  to form  $Ni$ , which has an activation energy of  $\sim 110$  kJ/mol.

The DSC method only allows measurements with low heating (0.02 - 1 K/s) rates. This is usually not the case for SCS reactions, which have much higher heating rates (100-5,000 K/s) for materials within the combustion wave [31]. González-Cortés and Imbert applied the Kissinger model to temperature-time histories (temperature profiles) for the *nickel*

*nitrate–urea* system [45]. After impregnating reactive solutions on alumina, the resulting solid mixture was heated at different rates ( $\beta = 0.016 - 0.166 \text{ K/s}$ ) to initiate the combustion. Such an approach allows for the manipulation of maximum combustion temperature ( $T_c$ ) in the 578 – 613 K range. The slope of the  $\ln(\beta/T^2) - 1/T$  graph yields the activation energy (176 kJ/mol).

Several mathematical approaches proposed by Zenin et al. [46] and Boddington et al. [47] have been used for temperature profile analyses to measure kinetic data in the CS processes. The method proposed by Zenin et al. uses the heat balance equation for self-sustaining reactions and utilizes the initial stages of the temperature profile. In order to determine the activation energy, the temperature profiles, combustion velocity, and the degree of conversion should be varied either by diluent (typically the product of the combustion reaction) or the preheating of the reactants to the ignition temperature of the system. The heat of reaction, the heat capacity, the thermal conductivities of products and reactants, along with the sample density should be accounted for in the calculation of the degree of conversion. However, these thermophysical parameters cannot be readily obtained for SCS systems, which makes the use of this approach challenging.

The combustion profile analysis method proposed by Boddington et al. utilizes the heat balance equation, which also includes the heat-transfer coefficient [47,48]. This approach employs the more advanced stages of the temperature profile (final stages of conversion). The use of this method in CS is preferable since there is no need for determination of the thermophysical parameters. Marinšek et al. applied this approach for a combustible citrate–nitrate system to produce  $\text{NiO–Y}_2\text{O}_3\text{–ZrO}_2$  [49]. The different quantities of alumina additions to the precursor enable manipulations of the combustion temperatures and wave propagation velocities. Such an approach yields an apparent activation energy of 61.4 kJ/mol. Marinšek also used this technique to determine activation energy (31.8 kJ/mol) for a similar system to produce a complex La- and Sr-based perovskite [50]. The validity of this model to describe the

kinetics of SCS reactions is questionable. It assumes that the combustion velocity, heat capacity, thermal conductivity, and density are constant during the combustion wave propagation [47,48].] Unlike the CS processes, the thermophysical parameters and densities of samples change during the SCS reactions. Moreover, in SCS reactions, drastic local temperature oscillations occur due to rapid gas release and a substantial increase in porosity. These conditions require smoothing of the temperature profiles before obtaining their first and second derivatives to compute the degree of conversion [49]. The use of such smoothing algorithms significantly influences the precision of measured activation energy values.

Correlating of the maximum combustion temperature ( $T_c$ ) and the combustion wave propagation velocity ( $V_c$ ) is a more broadly used approach for determining the activation energy ( $E$ ) of the CS reaction [43,51–53]. Zeldovich and Frank-Kamenetsky first developed a model correlating velocity and temperature for one-dimensional combustion wave propagation in gaseous systems. Merzhanov and Khaikin later adopted this model for solid-state systems [54,55]. The approach uses the following relationship:

$$\frac{V^2}{T_c^2} = f(\eta) K_0 \alpha \frac{c}{Q_0} \frac{R}{E} \exp\left(-\frac{E}{RT_c}\right) \quad (\text{eq. 1})$$

where  $f(\eta)$  is the kinetic law of the reaction,  $K_0$  is an arbitrary constant,  $\alpha$  is the thermal diffusivity of the product,  $Q_0$  is the heat of reaction, and  $R$  is the universal gas constant. In the approximation of a narrow reaction zone, the  $f(\eta)$  is constant and the natural logarithm of this equation takes the following form:

$$\ln\left(\frac{V}{T_c}\right) = A - \frac{E}{2RT_c} \quad (\text{eq. 2})$$

where the term  $A$  represents all constant values in narrow reaction zones. The slope of the  $\ln(V/T_c) - 1/T_c$  plot then allows for the determination of the activation energy. Multiple trials with different amounts of diluent are needed to generate combustion parameter datasets. The

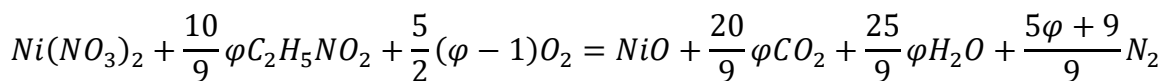
use of either a pyrometer or thin thermocouples (inserted in the samples) allow necessary measurements of temperature profiles and wave propagation velocities.

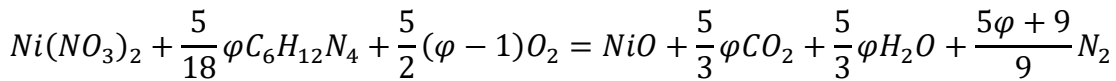
This work reports on a systematic study of the thermodynamics and kinetics of SCS reactions. The systems studied in this work involve  $\text{Ni}(\text{NO}_3)_2$ , an oxidizer, and either glycine ( $\text{C}_2\text{H}_5\text{NO}_2$ ) or hexamethylenetetramine (HMT,  $\text{C}_6\text{H}_{12}\text{N}_4$ ) as fuels. The use of the Gibbs free energy minimization principle allows for the simultaneous calculation of the  $T_{ad}$  and the composition of equilibrium products. This calculation reveals the influence of the  $\varphi$  ratio, amount of water, and oxygen in air on the  $T_{ad}$  and the composition of products. The measured combustion temperature and phase composition of products are compared with the results of thermodynamic calculations. Variations of drying times for solutions yield precursor gels with different water contents. This approach enables us to manipulate the combustion parameters and to determine the activation energies using the Merzhanov-Khaikin method.

## 2. Experimental

### 2.1. Thermodynamic Calculations

Simultaneous calculations of  $T_{ad}$  and composition of equilibrium products for the  $\text{Ni}(\text{NO}_3)_2 - \text{C}_2\text{H}_5\text{NO}_2 - \text{H}_2\text{O}$  and  $\text{Ni}(\text{NO}_3)_2 - \text{C}_6\text{H}_{12}\text{N}_4 - \text{H}_2\text{O}$  was conducted by THERMO software. For the determination of the equilibrium state, this program searches for the minimum of the Helmholtz or Gibbs free energy thermodynamic potentials accounting for the contributions of all initial reactants. THERMO contains a database that includes heat capacities (and their temperature dependencies) for possible gaseous and condensed phase products. For revealing the effect of  $\varphi$  ratio (changed from 0.1 – 3 range) the following two reactions were considered:





In the first set of calculations, the contribution of oxygen was accounted only for  $\varphi > 1$ , while in the second dataset, the contribution of oxygen was not considered. The parameter includes the number of  $H_2O$  moles (n), which were varied between 0 to 6 in both datasets. The calculations were performed in a constant ambient pressure regime. The calculated  $T_{ad}$  and molar quantities of major gases ( $CO_2$ ,  $CO$ ,  $N_2$ ,  $NO$ ,  $H_2O$ ,  $H_2$ ,  $O_2$ ,  $CH_4$ , and  $NH_3$ ) and condensed products ( $NiO$ ,  $Ni$ , and  $C$ ) were plotted as a function of  $\varphi$  and n values.

## 2.2. SCS experiments and Materials Characterization

The reactants used in this study are nickel nitrate hexahydrate ( $Ni(NO_3)_2 \cdot 6H_2O$ ; Alfa Aesar, 98%), glycine (Sigma, 99.5%), and HMT (Sigma, 99%). In the first set of experiments, the reactants with different  $\varphi$  ratios were dissolved in deionized water and mixed using a magnetic stirrer. The solutions were then heated on a hot plate to investigate the reactions in volume combustion mode. Several K-type thermocouples (100  $\mu m$  diameter) were inserted in the solutions to record temperature-time profiles with a 600 Hz frequency of measurements. The solutions were preheated to the boiling point of the solvent (Figure 1A). The evaporation of water took a long time and produced a gel-type substance. After evaporation of the solvent, combustion initiated in the entire volume of gel, and temperature rapidly rises from ignition point ( $T_{ig}$ ) to a maximum value ( $T_c$ ) followed by the cooling stage.

Combustion reactions in the self-propagating mode were utilized for calculations of activation energies. The reactive solutions were prepared first by dissolving an oxidizer and fuel with appropriate  $\varphi$  ratios in deionized water and thoroughly stirred. The obtained solutions were poured into a boat (50 mm in length, 10 mm width, and 10 mm height) and dried at 373 K for the different durations (3-7 h) to evaporate the solvent and produce the gels. *It is to be*

warned that gels with  $C_6H_{12}N_4$  react very vigorously. The drying temperature should not exceed 400 K to prepare such gels. The combustion reaction was initiated by the local preheating of gels in the air by a resistively heated tungsten wire. After initiation, the reaction propagated through the gels in the form of a moving combustion wave. Several thermocouples inserted inside the reactive gels allowed recording the time-temperature profiles of the process. The front propagation velocities were determined by dividing the distance between thermocouples (D) to temporal distance between thermocouple signals ( $\tau$ , see Figure 1B). In most cases, the uncertainty of the measured data for combustion temperature and velocity are 1-2 % and 5-8 %, respectively.

The phase compositions of the products were investigated by X-ray diffraction (XRD) using D8 Advance (Bruker) diffractometer operated at 40 kV and 40 mA with Cu  $K\alpha$  radiation. Step-scan size of 0.02° and counting times of 3 s were recorded for the angular range of 20–80°. A Magellan 400 (FEI) scanning electron microscope (SEM) is employed to characterize the morphology of the SCS products. The nitrogen adsorption-desorption analysis (at 77K) is performed to measure the specific surface area of the products using the ASAP 2020 instrument (Micromeritics). Before this analysis, the samples were vacuum degassed at 380 K for 6 h.

### 3. Results

#### 3.1. Thermodynamics

Figure 2 shows the results of the thermodynamic analysis for the  $Ni(NO_3)_2 + \frac{10}{9}\varphi C_2H_5NO_2 + \frac{5}{2}(\varphi - 1)O_2 + nH_2O$  system. In this calculation, oxygen was accounted only for  $\varphi > 1$  system. The n value was changed from 0 to 6 moles to model the maximum number of water in the nickel nitrate hexahydrate. The general trend is that an increase in the  $\varphi$  value

results in gradual increase of  $T_{ad}$  at any water content in the system. The highest calculated  $T_{ad}$  is 2480 K with  $\varphi = 3$  and  $n=0$ .

Figure 2 also shows concentration plots for primary products of the reaction. The equilibrium quantities of  $\text{CO}_2$  and  $\text{N}_2$  along with water vapor (not shown) increase with increasing ratio of  $\varphi$  for every given value of  $n$ . The oxygen concentration is steadily decreasing with increasing  $\varphi$  values all the way to  $\varphi \sim 1$ . The oxygen content has minimal values at the darker blue area on the level plot. Fuel-rich system ( $\varphi > 2$ ) with a small amount of water ( $n < 3$ ) yields slightly higher concentrations of oxygen. Although molecular nitrogen is dominant in most products, some  $\text{NO}$  also forms in the fuel-rich system. The same trend is also true for  $\text{CO}$ , even though the  $\text{CO}/\text{CO}_2$  ratio is almost five times greater than the  $\text{NO}/\text{N}_2$  one. The gas products for the fuel-rich system also contain a small quantity (up to 0.19 mole) of hydrogen.

The level plots indicate that  $\text{NiO}$  is the main solid product of the reaction for large  $\varphi$  and  $n$  parametric areas. Interestingly,  $\text{NiO}$  is present in every calculated product. Even the products for fuel-rich solutions (red area in  $\text{Ni}$  level plot,  $\varphi > 2$ ,  $n < 3$ ) contain some molten  $\text{NiO}$  along with  $\text{Ni}$  as the main product. The latter is also mostly in the molten state in this area, along with some vapor and solid nickel. The calculations also suggest that volatile  $\text{NiOH}$  (not shown) form when  $\varphi > 2$  and  $n < 3$  due to the high reaction temperature. The result of this calculation suggests that in the fuel-rich solution, the molecular oxygen incorporated into the system mostly favors the formation of  $\text{NiO}$ .

To assess the influence of oxygen on equilibrium product composition, a set of calculations were conducted for the  $\text{Ni}(\text{NO}_3)_2 + \frac{10}{9}\varphi \text{C}_2\text{H}_5\text{NO}_2 + n\text{H}_2\text{O}$  system. Figure 3 summarizes the plot for  $T_{ad}$  and products' molar compositions. The results for  $\varphi \leq 1$  are identical to the case of Figure 2 for the same  $\varphi$  ratios. These calculations indicate a different behavior for  $T_{ad}$  for solutions with  $\varphi > 1$ . The highest adiabatic temperature (2000 - 2230 K) can be found

in the vicinity of  $\varphi \approx 1$  when  $n \approx 0$  (red area on the  $T_{ad}$  plot). In most other cases, the temperature gradually decreases with increasing both variables. The concentrations of  $\text{CO}_2$  and  $\text{N}_2$  along with water vapor (not shown) also gradually increase with the growth of  $\varphi$  ratio in the given value of  $n$  parameter.  $\text{NO}$  gas in small quantities also forms, and its formation correlates well with the combustion temperatures. The higher the temperature, the higher the quantity of  $\text{NO}$  in the products. Unlike the previous case, the fuel-rich system forms considerable quantities of reducing gases ( $\text{CO}$ ,  $\text{H}_2$ ,  $\text{NH}_3$ , and  $\text{CH}_4$ ). The highest amounts of  $\text{CO}$  and  $\text{H}_2$  are found in the fuel-rich system when  $n \approx 0$ . In contrast, the highest concentrations of  $\text{CH}_4$  and  $\text{NH}_3$  are observed at  $n \approx 6$ . Nickel is the sole solid product of the system when  $1.2 < \varphi < 2.8$ , as the reaction temperatures are below its melting point. Figure 3 suggests that some carbon also forms along with  $\text{Ni}$  when  $\varphi > 2.8$ .

The results of the similar calculations for  $\text{Ni}(\text{NO}_3)_2 + \frac{5}{18}\varphi\text{C}_6\text{H}_{12}\text{N}_4 + \frac{5}{2}(\varphi - 1)\text{O}_2 + n\text{H}_2\text{O}$  and  $\text{Ni}(\text{NO}_3)_2 + \frac{5}{18}\varphi\text{C}_6\text{H}_{12}\text{N}_4 + n\text{H}_2\text{O}$  systems are summarized in Supplementary Figures S1 and S2, respectively. In general, trends are similar to the glycine case. The significant difference is that the adiabatic temperatures are  $\sim 300$  K higher for the HMT-containing systems. This causes some differences in product distributions. For example, the quantities of volatile  $\text{NiOH}$  are higher in some cases, which alerts the  $\text{Ni}/\text{NiO}$  ratio. The same is true for  $\text{CO}/\text{CO}_2$  and  $\text{NO}/\text{N}_2$  ratios.

### 3.2. Experimental validation of thermodynamic calculations

To validate the thermodynamic results, we measured the maximum temperature values ( $T_c$ ) of combustion profiles in volume combustion mode. Several trials were conducted to obtain the average value of  $T_c$  as a function of  $\varphi$  ratios. Figure 4 shows the behavior of  $T_c$  as a function of  $\varphi$  for both fuels (blue data points). Figure 4A shows that for glycine-containing solutions,  $T_c$  gradually increases from  $\sim 500$  to  $1250$  K when  $\varphi$  increases from 0.3 to 1.25.

Further increase of the  $\phi$  ratio to 3 results in a steady decrease in the combustion temperature to  $\sim 750$ K. Solutions with higher  $\phi$  ratio do not react in self-sustaining mode.

Figure 4 also illustrates two sets of values for  $T_{ad}$  with different amounts of water ( $n$ , moles) in the system. One set of data (dashed lines) models the case for the presence of molecular oxygen from the air. In contrast, the set of solid lines represents the case when the oxygen was excluded for calculating  $T_{ad}$ . Benchmarking the measured  $T_c$  data against these types of calculations, we can suggest that the  $T_c$  behavior is similar to the calculated  $T_{ad}$  when molecular oxygen was excluded from the system. However, the peak temperature is experimentally observed at a  $\phi$  ratio of 1.25, while the maximum values for the adiabatic temperature are at  $\phi=1$ .

The temperature profiles for glycine-contained solutions reveal that the ignition temperature of the process is  $440\pm 10$  K for all  $\phi$  ratios. Early reports on DSC data [56,57] show that nickel nitrate hexahydrate releases almost four molecules of water at 430-450 K. These facts suggest an  $n$  value of  $\sim 2$  before the ignition of the combustion process. Comparing  $T_c$  with  $T_{ad}$  calculated at  $n=2$ , we can see that the difference is almost 500 K. Such significantly low values for combustion temperatures can be attributed to thermal losses during experiments.

There is, however, an even more significant deviation of  $T_c$  from  $T_{ad}$  values for the HMT-containing system (Figure 4B). Taking into account that the ignition temperature is  $470\pm 10$  K, the gels could contain 1-2 moles of bound water. Based on this, we estimate that difference between  $T_c$  and  $T_{ad}$  can be as high as 900 K for most of the  $\phi$  ratios (Figure 4B). Such a significant deviation from adiabatic conditions can be related to the fact that the combustion process for the HMT-based solutions proceeds more vigorously than glycine-containing solutions. Another difference in the HMT system is the absence of a clearly defined peak temperature for  $T_c - \phi$  plot.

We also compared the compositions of analyzed solid-state products for both systems with the thermodynamically predicted compositions. XRD patterns for products of fuel-lean ( $\phi \leq 1$ ) glycine-containing solutions consist of mainly NiO (Figure 5A), while fuel-rich solutions ( $\phi \geq 1.25$ ) results in Ni phase. This result is in good agreement with the thermodynamically predicted composition of products for the case of the exclusion of the molecular oxygen from the calculations (Figure 3).

XRD analysis of products for HMT-containing solutions shows a different trend. Fuel-lean solutions ( $\phi < 1$ ) results in pure NiO, whereas at the  $1 \leq \phi < 2$  range, the Ni-NiO composites form as products (Figures 5B and S3). Nearly pure-phase Ni can be obtained only at  $\phi \geq 2$  (Figure 5B). These results are in disagreement with both cases of thermodynamic simulations presented in Figures S1 and S2. Such disagreements could be related to the fact that the combustion of HMT-containing solutions proceeds vigorously, which seemingly forms products far away from equilibrium conditions.

SEM images of the selected product for combusted solutions also reflect differences in the combustion behavior of both fuels. NiO formed at the combustion of glycine-lean ( $\phi = 0.75$ ) solution exhibit a porous structure with sub-micrometer size pores (Figure 6). The sizes of individual grains are below 100 nm. At  $\phi = 1.25$ , the product is less porous and contains irregular-shaped grains with sizes of 50 – 200 nm (Figure 6). SEM images for HMT-derived combustion products exhibit different microstructures. Both HMT-lean and HMT-rich solutions result in products with large agglomerates of fine nanoscale particles with sizes below 100 nm.

Surface area measurements of product powders also show significant distinctions for both fuels. NiO produced by combusting glycine-lean solution has a  $6.5 \text{ m}^2/\text{g}$  surface area, while for NiO obtained from the HMT-lean solution, this parameter is  $31.3 \text{ m}^2/\text{g}$ . The surface

areas for Ni prepared by glycine- and HMT-rich solutions are 0.39 and 4.87 m<sup>2</sup>/g, respectively. Table 1 summarizes the combustion temperatures for some solutions and surface areas of the corresponding materials. Combustion temperatures for HMT-based solutions are lower than for glycine solutions. Low reaction temperatures for HMT fuel results in a higher specific area. However, temperature differences alone may not be enough to explain such sizeable microstructural differences. Therefore, the role of specific durations for the reactions and gas release rates could become an essential factor in determining the products' microstructural features.

### 3.3. Kinetics of the Processes

To measure the combustion wave velocities and determine the activation energies, we use the self-propagation mode of SCS reactions. Four types of gels with different quantities of water were prepared by drying solutions with different times (3-7 h) at 373 K. The combustion reaction was initiated by the local preheating of gels, and temperature profiles, as well as the wave propagation velocities, were measured using thermocouples.

Figure 7 summarizes the combustion temperatures and wave propagation velocities as a function of drying time for all types of gels. The general trend for all four gels is that increasing the drying time increases both T<sub>c</sub> and V. An exception is an HMT-rich gel ( $\phi=2.25$ ) prepared by seven hours of drying (Figure 7B). Such a decrease related to the fact that HMT-gels react vigorously. In these cases, the reacting samples lose their integrity due to the local eruptions, which could slow the wave propagation. Figure 7 shows that the wave propagation velocity for the HMT system is, on average, 3-4 times higher than that of glycine gels. This fact points out that the specific reaction times for HMT-based gels are significantly shorter than glycine-containing gels. Another difference is that the combustion temperature for fuel-rich

systems forming nickel is higher for the glycine in contrast to HMT. For the fuel-lean system producing NiO, the opposite trend is observed (Figure 7).

Variation of drying times allows for obtaining precursor gels with different water content. This approach enables the manipulation of the combustion parameters and determination of the activation energies for different systems using the Merzhanov-Khaikin method. The measured combustion parameters are used to construct Arrhenius-type plots of  $\ln(V/T_c)$  against  $1/T_c$  for four solutions (Figure 8). These plots indicate the existence of a linear relationship between the combustion parameters across a wide temperature range (150-300 K). Linear fitting of these data points allows determining the activation energies for NiO and Ni formation processes for two fuels (Figure 8 and Table 1).

#### 4. Discussion

The commonly used method [58–61] for the thermodynamic consideration of SCS processes that allows predicting the magnitude of the temperatures during an adiabatic process uses the principle of equality of enthalpy for the final products ( $\Delta H_p^0$ ) at  $T_{ad}$  and the enthalpy ( $H^0(T_0)$ ) reactants in the initial temperature ( $T_0$ ):

$$\sum \Delta H^0(T_0) = \sum \Delta H_{products}^0(T_{ad})$$

This principle allows deducing a simple relationship

$$T_{ad} = T_0 + \frac{\Delta H^0}{C_p}$$

where  $C_p$  is the temperature-dependent heat capacity (mean value) at the  $T_0$  -  $T_{ad}$  range. The previous works using this approach assume that only  $\text{CO}_2$ ,  $\text{N}_2$ ,  $\text{H}_2\text{O}$ , and metal oxide products form during SCS. Besides, it assumes that the solid-state product does not melt below  $T_{ad}$  as no enthalpy of melting is incorporated in the equation. These calculations also assume that no side reactions take place and that a stoichiometric reaction occurs during the process.

The thermodynamic modeling approach used in the present work determines the equilibrium state and  $T_{ad}$  simultaneously in a sizeable parametric space. Our calculations are based on the search of the minimum value for the Gibbs free energy accounting for all contributions of the oxidizer, fuel, and solvent. The calculations reveal that at different  $\phi$  ratios, CO, CH<sub>4</sub>, NH<sub>3</sub>, NO, as well as gas-phase nickel hydroxides along with Ni, NiO, CO<sub>2</sub>, N<sub>2</sub>, and H<sub>2</sub>O form. This in-depth knowledge of realistic equilibrium compositions is valuable in the optimization of the processes for the preparation of materials in larger scales.

However, there is a significant deviation in measured  $T_c$  and calculated  $T_{ad}$  values, especially for solutions with HMT fuel. Such deviations suggest that in some systems, SCS can proceed far from thermodynamically predicted equilibrium conditions. Alternatively, there should be other processes that we cannot account in the calculations. The composition of solid-state material obtained with glycine fuel are in a good agreement with thermodynamically predicted products. For HMT-based solutions, the product compositions differ from calculations. We can assume that the rapid release of a significant amount of gas reduces the reaction temperature within the wave. Such a decrease, in turn, influences the composition and morphology of the resulting material. The practical benefit of such differences is that by a simple change in fuel type, one could significantly tailor the morphology and properties of reaction products.

This work also presents the first use of the Merzhanov-Khaikin approach to determine the activation energy of SCS processes. Our results show that higher activation energies characterize reactions in fuel-lean systems that produce the NiO. For example, in the glycine-containing solutions, the activation energy for NiO formation is almost twice as high as the one forming Ni. This result is qualitatively in agreement with the earlier reported activation energy by Kumar et al. using the Kissinger-based treatment of DSC results. The differences between energies for Ni and NiO synthesis in the HMT-based gels are not as high as the ones involving

glycine. The uncertainties of activation energy determination in HMT-based system are also higher due to the measurement uncertainties of the combustion parameters. Nevertheless, in both fuels, the activation energies for Ni formation processes, are lower.

The effective (apparent) activation energies reported in this work characterize macroscopic kinetics of the combustion even if accounting for heat and mass transfer processes. However, we can assume that the determined energy values could be correlated with some rate-limiting stages in the sequence of reactions that are responsible for the combustion wave propagation. Previously reported works suggest several possible mechanisms of SCS. For example, in  $\text{Ni}(\text{NO}_3)_2$  + glycine system, the highly exothermic reaction between the decomposition products of oxidizer and fuel ( $\text{N}_2\text{O}$  and  $\text{NH}_3$ , respectively) could be responsible for the combustion wave propagation in fuel-lean solutions [57]. On the other hand, the availability of these gas-phase intermediates primarily depends on the decomposition rates for the initial reactants. The activation energy for decomposition of “anhydrous nickel nitrate” (prepared by the isothermal heating of the  $\text{Ni}(\text{NO}_3)_2 \cdot 6\text{H}_2\text{O}$  at 423 K) in air was found to be in the 143.1 - 152.8 kJ/mol range [62]. The activation energy for glycine decomposition in nitrogen is 158.29 kJ/mol [63]. We can suggest that such high values make the reactants’ decompositions rate-limiting stages, which could be translated into relatively higher activation energies for the combustion of fuel-lean systems.

The decomposition of a coordination complex compound was also identified as another mechanism for the combustion of the  $\text{Fe}(\text{NO}_3)_3$  + HMT fuel-rich gels [8]. In fact, a complex compound,  $(\text{NO}_3)_2\text{Ni}(\text{H}_2\text{O})_6(\text{HMT})_2 \cdot 4\text{H}_2\text{O}$ , between nickel nitrate and HMT was isolated earlier [64]. Thermal decomposition of this material is exothermic, and the process accompanies a rapid release of  $\text{CO}$ ,  $\text{N}_2$ , and  $\text{H}_2\text{O}$  gases at 323 - 550 K. The decomposition product of this complex is Ni with some carbon impurities. Based on these facts, we can suggest that the ignition of the combustion process and kinetics of fuel-rich mixtures may be

determined by the thermal decomposition features of such coordinated compounds. We can also postulate that decomposition of complexes could be characterized by relatively lower activation energies. Indeed, the intramolecular redox reaction involving nitrate and amine groups would require lower activation energies in contrast to the decomposition of individual reactants. We can suggest that in both systems, with fuel-rich gels, the decomposition of such coordinated compounds are responsible for lower activation energies (Figure 8). The rapid nature of the SCS method makes the investigation of such molecular mechanisms a challenging task. Therefore, more researches are needed to explore those mechanisms and reveal their relations to the kinetics of combustion processes.

## Conclusions

This work presents a systematic investigation of thermodynamics and kinetics of SCS reactions in systems that involve nickel nitrate, as an oxidizer, and either glycine or hexamethylenetetramine as fuels. The use of an approach based on Gibbs free energy minimization principle allowed for accurate thermodynamic modeling of systems. These calculations reveal the effects of fuel-to-oxidizer ratio, oxygen in the air, and water quantities of adiabatic combustion temperatures and equilibrium compositions of product in a sizable parametric space. The experimental investigations show significantly lower measured combustion temperatures in comparison to calculated adiabatic combustion temperatures resulting from heat losses. Compositions of analyzed NiO or Ni products for glycine-containing solutions revealed good agreement with the thermodynamically predicted composition of products for the case of the exclusion of the molecular oxygen from the calculations. In HMT-based solutions, nickel can be obtained in much higher fuel-to-oxidizer ratios compared to thermodynamic predictions. This deviation is related to rapid gas-phase product removal from the combustion zone, which forms products far away from equilibrium conditions. The use of the Merzhanov-Khaikin approach to determine the activation energies reveals that the

combustion of fuel-lean solutions is characterized by higher activation energies than the fuel-rich cases. Reduction in activation energies due to the increase in the fuel-to-oxidizer ratio could be related to changes in the rate-limiting stages from the endothermic decomposition of individual reactants to exothermic decomposition of coordinate compounds formed between the reactants.

### Acknowledgments

The work was performed with financial support in parts from the U.S. Department of Energy's (DOE) National Nuclear Security Administration (NNSA, Grant # DE-NA0003888), U.S. National Science Foundation (NSF, PHY-1713857), JINA-CEE NSF Physics Frontiers Centers (Award #:1430152) and the Committee of Science of the Republic of Armenia (Project #18T-1D051). A. Aprahamian acknowledges support from the Fulbright U.S. Scholar grant.

### References

- [1] A. Varma, A.S. Mukasyan, A.S. Rogachev, K.V Manukyan, Solution Combustion Synthesis of Nanoscale Materials, *Chem. Rev.* 116 (2016) 14493–14586.
- [2] S. Specchia, G. Ercolino, S. Karimi, C. Italiano, A. Vita, Solution combustion synthesis for preparation of structured catalysts: A mini-review on process intensification for energy applications and pollution control, *Int. J. Self Propag. High Temp. Synth.* 26 (2017) 166–186.
- [3] K. Rajeshwar, N.R. de Tacconi, Solution combustion synthesis of oxide semiconductors for solar energy conversion and environmental remediation, *Chem. Soc. Rev.* 38 (2009) 1984–1998.
- [4] T. Mokkelbost, I. Kaus, T. Grande, M.A. Einarsrud, Combustion synthesis and characterization of nanocrystalline CeO<sub>2</sub>-based powders, *Chem. Mater.* 16 (2004) 5489–5494.
- [5] K.V. Manukyan, Y.-S. Chen, S. Rouvimov, P. Li, X. Li, S. Dong, X. Liu, J.K. Furdyna, A. Orlov, G.H. Bernstein, W. Porod, S. Roslyakov, A.S. Mukasyan, Ultrasmall  $\alpha$ -Fe<sub>2</sub>O<sub>3</sub> superparamagnetic nanoparticles with high magnetization prepared by template-assisted combustion process, *J. Phys. Chem. C* 118 (2014) 16264–16271.
- [6] Y. Wang, J. Zeng, Y. Peng, J. Li, Y. Zhang, H. Li, J. Zhao, Ultrafast one-pot air atmospheric solution combustion approach to fabricate mesoporous metal sulfide/carbon composites with enhanced lithium storage properties, *ACS Appl. Energy Mater.* 1 (2018) 6190–6197.
- [7] N. Ardebilchi Marand, S.M. Masoudpanah, M.Sh. Bafghi, S. Alamolhoda, Photocatalytic activity of nickel sulfide composite powders synthesized by solution combustion method, *J. Electron. Mater.* 49 (2020) 1266–1272.
- [8] A.S. Mukasyan, S. Roslyakov, J.M. Pauls, L.C. Gallington, T. Orlova, X. Liu, M. Dobrowolska, J.K. Furdyna, K.V. Manukyan, Nanoscale metastable  $\varepsilon$ -Fe<sub>3</sub>N ferromagnetic materials by self-sustained reactions, *Inorg. Chem.* 58 (2019) 5583–5592.
- [9] A. Kumar, E.E. Wolf, A.S. Mukasyan, Solution combustion synthesis of metal

nanopowders: Nickel—reaction pathways, *AIChE J.* 57 (2011) 2207–2213.

- [10] G.R. Rao, B.G. Mishra, H.R. Sahu, Synthesis of CuO, Cu and CuNi alloy particles by solution combustion using carbohydrazide and N-tertiarybutoxy-carbonylpiperazine fuels, *Mater. Lett.* 58 (2004) 3523–3527.
- [11] A.S. Prakash, P. Manikandan, K. Ramesha, M. Sathiya, J.-M. Tarascon, A.K. Shukla, Solution-combustion synthesized nanocrystalline  $\text{Li}_4\text{Ti}_5\text{O}_{12}$  as high-rate performance Li-Ion battery anode, *Chem. Mater.* 22 (2010) 2857–2863.
- [12] L. Sharma, A. Bhatia, L. Assaud, S. Franger, P. Barpanda, Ultra-rapid combustion synthesis of  $\text{Na}_2\text{FePO}_4\text{F}$  fluorophosphate host for Li-ion and Na-ion insertion, *Ionics* 24 (2018) 2187–2192.
- [13] F. Li, J. Ran, M. Jaroniec, S.Z. Qiao, Solution combustion synthesis of metal oxide nanomaterials for energy storage and conversion, *Nanoscale* 7 (2015) 17590–17610.
- [14] C. Galletti, S. Specchia, G. Saracco, V. Specchia, CO-selective methanation over Ru- $\gamma\text{Al}_2\text{O}_3$  catalysts in H<sub>2</sub>-rich gas for PEM FC applications, *Chem. Eng. Sci.* 65 (2010) 590–596.
- [15] B. Wang, L. Zeng, W. Huang, F.S. Melkonyan, W.C. Sheets, L. Chi, M.J. Bedzyk, T.J. Marks, A. Facchetti, Carbohydrate-assisted combustion synthesis to realize high-performance oxide transistors, *J. Am. Chem. Soc.* 138 (2016) 7067–7074.
- [16] J. Li, Y.H. Zhou, W.Q. Zhu, J.H. Zhang, Z.L. Zhang, Combustion synthesis of nontoxic water-induced InYO thin film and application in thin film transistor, *Mater. Sci. Semicond. Process.* 93 (2019) 201–207.
- [17] P. Bera, M.S. Hegde, Characterization and catalytic properties of combustion synthesized Au/CeO<sub>2</sub>, *Catal. Letters.* 79 (2002) 75–81.M.K.
- [18] Hossain, E. Kecsenovity, A. Varga, M. Molnár, C. Janáky, K. Rajeshwar, Solution combustion synthesis of complex oxide semiconductors, *Int. J. Self Propag. High Temp. Synth.* 27 (2018) 129–140.
- [19] M.Y. Nassar, T.Y. Mohamed, I.S. Ahmed, I. Samir, MgO nanostructure via a sol-gel combustion synthesis method using different fuels: An efficient nano-adsorbent for the removal of some anionic textile dyes, *J. Mol. Liq.* 225 (2017) 730–740.
- [20] M. Ahmad, E. Ahmed, Y. Zhang, N.R. Khalid, J. Xu, M. Ullah, Z. Hong, Preparation of highly efficient Al-doped ZnO photocatalyst by combustion synthesis, *Curr. Appl. Phys.* 13 (2013) 697–704.
- [21] D.E. Wagner, K.M. Eisenmann, A.L. Nestor-Kalinowski, S.B. Bhaduri, A microwave-assisted solution combustion synthesis to produce europium-doped calcium phosphate nanowhiskers for bioimaging applications, *Acta Biomater.* 9 (2013) 8422–8432.
- [22] M. Nabiyouni, H. Zhou, S.B. Bhaduri, Microwave assisted solution combustion synthesis (MASCS) of europium (Eu) doped chlorapatite nanowhiskers, *Mater. Lett.* 108 (2013) 54–57.
- [23] A.G. Merzhanov, The chemistry of self-propagating high-temperature synthesis, *J. Mater. Chem.* 14 (2004) 1779–1786.
- [24] K. Manukyan, D. Davtyan, J. Bossert, S. Kharatyan, Direct reduction of ammonium molybdate to elemental molybdenum by combustion reaction, *Chem. Eng. J.* 168 (2011) 925–930.
- [25] K. Morsi, Combustion synthesis and electric field: A review, *Int. J. Self Propag. High Temp. Synth.* 26 (2017) 199–209.
- [26] K. V. Manukyan, R.S. Schools, A.S. Mukasyan, Size-tunable germanium particles prepared by self-sustaining reduction of germanium oxide, *J. Solid State Chem.* 270 (2019) 92–97.
- [27] K.V. Manukyan, Combustion and materials synthesis, *Int. J. Self Propag. High Temp. Synth.* 26 (2017) 143–144.
- [28] W. Wen, J.M. Wu, Nanomaterials via solution combustion synthesis: A step nearer to

controllability, *RSC Adv.* 4 (2014) 58090–58100.

- [29] S.T. Aruna, A.S. Mukasyan, Combustion synthesis and nanomaterials, *Curr. Opin. Solid State Mater. Sci.* 12 (2008) 44–50.
- [30] K. Deshpande, A. Mukasyan, A. Varma, Direct synthesis of iron oxide nanopowders by the combustion approach: Reaction mechanism and properties, *Chem. Mater.* 16 (2004) 4896–4904.
- [31] H.H. Nersisyan, J.H. Lee, J.R. Ding, K.S. Kim, K.V. Manukyan, A.S. Mukasyan, Combustion synthesis of zero-, one-, two- and three-dimensional nanostructures: Current trends and future perspectives, *Prog. Energy Combust. Sci.* 63 (2017) 79–118.
- [32] P. Bera, Solution combustion synthesis as a novel route to preparation of catalysts, *Int. J. Self Propag. High Temp. Synth.* 28 (2019) 77–109.
- [33] R. Ianoş, R. Istratie, C. Păcurariu, R. Lazău, Solution combustion synthesis of strontium aluminate,  $\text{SrAl}_2\text{O}_4$ , powders: Single-fuel versus fuel-mixture approach, *Phys. Chem. Chem. Phys.* 18 (2015) 1150–1157.
- [34] C.O. Ehi-Eromosele, B.I. Ita, E.E.J. Iweala, Low-temperature combustion synthesis of cobalt magnesium ferrite magnetic nanoparticles: effects of fuel-to-oxidizer ratio and sintering temperature, *J. Sol-Gel Sci. Technol.* 76 (2015) 298–308.
- [35] V.B. Raghavendra, S. Naik, M. Antony, G. Ramalingam, M. Rajamathi, S. Raghavan, Amorphous, monoclinic, and tetragonal porous zirconia through a controlled self-sustained combustion route, *J. Am. Ceram. Soc.* 94 (2011) 1747–1755.
- [36] N. Srinatha, V. Dinesh Kumar, K.G.M. Nair, B. Angadi, The effect of fuel and fuel-oxidizer combinations on  $\text{ZnO}$  nanoparticles synthesized by solution combustion technique, *Adv. Powder Technol.* 26 (2015) 1355–1363.
- [37] S.M. Khaliullin, V.D. Zhuravlev, V.G. Bamburov, Solution-combustion synthesis of oxide nanoparticles from nitrate solutions containing glycine and urea: Thermodynamic aspects, *Int. J. Self Propag. High Temp. Synth.* 25 (2016) 139–148.
- [38] H. Parnianfar, S.M. Masoudpanah, S. Alamolhoda, H. Fathi, Mixture of fuels for solution combustion synthesis of porous  $\text{Fe}_3\text{O}_4$  powders, *J. Magn. Magn. Mater.* 432 (2017) 24–29.
- [39] R. Ianoş, R. Băbuță, C. Păcurariu, R. Lazău, R. Istratie, C. Butaciu, Combustion synthesis of  $\text{ZnAl}_2\text{O}_4$  powders with tuned surface area, *Ceram. Int.* 43 (2017) 8975–8981.
- [40] D.G. Kuvshinov, P.B. Kurmashov, A.G. Bannov, M.V. Popov, G.G. Kuvshinov, Synthesis of Ni-based catalysts by hexamethylenetetramine-nitrates solution combustion method for co-production of hydrogen and nanofibrous carbon from methane, *Int. J. Hydrogen Energy.* 44 (2019) 16271–16286.
- [41] A. Ashok, A. Kumar, R. Bhosale, M.A. Saleh Saad, F. AlMomani, F. Tarlochan, Study of ethanol dehydrogenation reaction mechanism for hydrogen production on combustion synthesized cobalt catalyst, *Int. J. Hydrogen Energy.* 42 (2017) 23464–23473.
- [42] J. Monnier, C. Rey, S. Chandra Mohan, J. Causse, E. Welcomme, X. Deschanel, Conversion of actinide nitrate surrogates into oxide using combustion synthesis process: A facile approach, *J. Nucl. Mater.* 525 (2019) 14–21.
- [43] A.S. Mukasyan, C.E. Shuck, Kinetics of SHS reactions: A review, *Int. J. Self Propag. High Temp. Synth.* 26 (2017) 145–165.
- [44] H.E. Kissinger, Reaction kinetics in differential thermal analysis, *Anal. Chem.* 29 (1957) 1702–1706.
- [45] L.S. González-Cortés, F.E. Imbert, Fundamentals, properties and applications of solid catalysts prepared by solution combustion synthesis (SCS), *Appl. Catal. A* 452 (2013) 117–131.
- [46] A.A. Zenin, A.G. Merzhanov, G.A. Nersisyan, Thermal wave structure in SHS processes,

Combust. Explos. Shock Waves. 17 (1981) 63–71.

[47] T. Boddington, P.G. Laye, J. Tipping, D. Whalley, Kinetic analysis of temperature profiles of pyrotechnic systems, *Combust. Flame* 63 (1986) 359–368.

[48] S.D. Dunmead, Z.A. Munir, J.B. Holt, Temperature profile analysis in combustion synthesis: I, Theory and Background, *J. Am. Ceram. Soc.* 75 (1992) 175–179.

[49] M. Marinšek, J. Kemperl, B. Likozar, J. Maček, Temperature profile analysis of the citrate-nitrate combustion system, *Ind. Eng. Chem. Res.* 47 (2008) 4379–4386.

[50] M. Marinšek, Analysis of the temperature profiles during the combustion synthesis of doped lanthanum gallate, *Mater. Tehnol.* 42 (2008) 85–91.

[51] H. Il Won, H.H. Nersisyan, C.W. Won, A macrokinetic study of the  $\text{WO}_3/\text{Zn}$  reaction diluted with  $\text{NaCl}$ , *Chem. Eng. J.* 153 (2009) 193–198.

[52] K.V. Manukyan, K.G. Kirakosyan, Y.G. Grigoryan, O.M. Niazyan, A.V. Yeghishyan, A.G. Kirakosyan, S.L. Kharatyan, Mechanism of molten-salt-controlled thermite reactions, *Ind. Eng. Chem. Res.* 50 (2011) 10982–10988.

[53] R. Tomasi, Z.A. Munir, Effect of particle size on the reaction wave propagation in the combustion synthesis of  $\text{Al}_2\text{O}_3\text{--ZrO}_2\text{--Nb}$  composites, *J. Am. Ceram. Soc.* 82 (1999) 1985–1992.

[54] B.I. Khaikin, A.G. Merzhanov, Theory of thermal propagation of a chemical reaction front, *Combust. Explos. Shock Waves* 2 (1966) 22–27.

[55] A.G. Merzhanov, B.I. Khaikin, Theory of combustion waves in homogeneous media, *Prog. Energy Combust. Sci.* 14 (1988) 1–98.

[56] W. Brockner, C. Ehrhardt, M. Gjikaj, Thermal decomposition of nickel nitrate hexahydrate,  $\text{Ni}(\text{NO}_3)_2\cdot 6\text{H}_2\text{O}$ , in comparison to  $\text{Co}(\text{NO}_3)_2\cdot 6\text{H}_2\text{O}$  and  $\text{Ca}(\text{NO}_3)_2\cdot 4\text{H}_2\text{O}$ , *Thermochim. Acta* 456 (2007) 64–68.

[57] K.V. Manukyan, A. Cross, S. Roslyakov, S. Rouvimov, A.S. Rogachev, E.E. Wolf, A.S. Mukasyan, Solution combustion synthesis of nano-crystalline metallic materials: mechanistic studies, *J. Phys. Chem. C* 117 (2013) 24417–24427.

[58] H. Aali, S. Mollazadeh, J.V. Khaki, Quantitative evaluation of ambient  $\text{O}_2$  interference during solution combustion synthesis process: considering iron nitrate – fuel system, *Ceram. Int.* 45 (2019) 17775–17783.

[59] H. Aliasghari, A.M. Arabi, H. Haratizadeh, A novel approach for solution combustion synthesis of tungsten oxide nanoparticles for photocatalytic and electrochromic applications, *Ceram. Int.* 46 (2020) 403–414.

[60] E. Yilmaz, M.S. Sonmez, The influence of process parameters on the chemical and structural properties of solution combustion prepared vanadium pentoxide, *Mater. Lett.* 261 (2020) 127095.

[61] S.M. Khaliullin, V.D. Zhuravlev, V.G. Bamburov, A.A. Khort, S.I. Roslyakov, G. V. Trusov, D.O. Moskovskikh, Effect of the residual water content in gels on solution combustion synthesis temperature, *J. Sol-Gel Sci. Technol.* 93 (2020) 251–261.

[62] B. Janković, S. Mentus, D. Jelić, A kinetic study of non-isothermal decomposition process of anhydrous nickel nitrate under air atmosphere, *Phys. B* 404 (2009) 2263–2269.

[63] M. Huang, S. Lv, C. Zhou, Thermal decomposition kinetics of glycine in nitrogen atmosphere, *Thermochim. Acta* 552 (2013) 60–64.

[64] P. Afanasiev, S. Chouzier, T. Czeri, G. Pilet, C. Pichon, M. Roy, M. Vrinat, Nickel and cobalt hexamethylentetramine complexes  $(\text{NO}_3)_2\text{Me}(\text{H}_2\text{O})_6(\text{HMTA})_2\cdot 4\text{H}_2\text{O}$  ( $\text{Me} = \text{Co}^{2+}, \text{Ni}^{2+}$ ): New molecular precursors for the preparation of metal dispersions, *Inorg. Chem.* 47 (2008) 2303–2311.

Table 1:

Combustion temperature, phase composition, specific surface areas, crystallite sizes determined by Scherrer equation of selected products and activation energy of SCS processes

Fuel	$\phi$	T <sub>c</sub> , K	Surface area, m <sup>2</sup> /g	Composition	Crystallite size, nm	Activation energy, kJ/mol
<b>Glycine</b>	0.75	900	6.5	NiO	78	107±13
	1.25	1305	0.39	Ni	105	54±8
<b>HMT</b>	0.75	750	31.3	NiO	23	140±18
	2.25	870	4.87	Ni	69	110±25

## Figure captions

Figure 1: A typical temperature - time profile for  $\text{Ni}(\text{NO}_3)_2 + \text{C}_6\text{H}_{12}\text{N}_4 + \text{H}_2\text{O}$  system (A) solution reacted in volume-combustion (A) and self-propagating (B) modes to measure maximum combustion temperature ( $T_c$ ) and the wave propagation velocity (V), where D is the distance between thermocouples in cm and  $\tau$  is the temporal distance of thermocouple signals in seconds.

Figure 2: Two-dimensional level plots for  $T_{ad}$  and equilibrium product for the  $\text{Ni}(\text{NO}_3)_2 + \frac{10}{9}\varphi\text{C}_2\text{H}_5\text{NO}_2 + \frac{5}{2}(\varphi - 1)\text{O}_2 + n\text{H}_2\text{O}$  system depend on  $\varphi$  ratio and n (number of moles for  $\text{H}_2\text{O}$ ).

Figure 3: Two-dimensional level plots for  $T_{ad}$  and equilibrium product for the  $\text{Ni}(\text{NO}_3)_2 + \frac{10}{9}\varphi\text{C}_2\text{H}_5\text{NO}_2 + n\text{H}_2\text{O}$  system depend on  $\varphi$  ratio and n values. Oxygen was not accounted.

Figure 4: Maximum combustion temperature ( $T_c$ , blue data points) versus  $\varphi$  ratio for the  $\text{Ni}(\text{NO}_3)_2 + \frac{10}{9}\varphi\text{C}_2\text{H}_5\text{NO}_2 + \text{H}_2\text{O}$  (A) and  $\text{Ni}(\text{NO}_3)_2 + \frac{5}{18}\varphi\text{C}_6\text{H}_{12}\text{N}_4 + \frac{5}{2}(\varphi - 1)\text{O}_2 + n\text{H}_2\text{O}$  (B) systems. Plots also include calculated  $T_{ad}$  values (solid and dashed lines).

Figure 5: XRD patterns of products for the  $\text{Ni}(\text{NO}_3)_2 + \frac{10}{9}\varphi\text{C}_2\text{H}_5\text{NO}_2$  (A) and  $\text{Ni}(\text{NO}_3)_2 + \frac{5}{18}\varphi\text{C}_6\text{H}_{12}\text{N}_4$  (B) prepared with different  $\varphi$  ratios.

Figure 6: SEM images of products for the  $\text{Ni}(\text{NO}_3)_2 + \frac{10}{9}\varphi\text{C}_2\text{H}_5\text{NO}_2$  and  $\text{Ni}(\text{NO}_3)_2 + \frac{5}{18}\varphi\text{C}_6\text{H}_{12}\text{N}_4$  systems prepared with different  $\varphi$  ratios. The scale bar is 500 nm for all images.

Figure 7: Maximum combustion temperature ( $T_c$ ) and wave propagation velocity (V) versus  $\varphi$  ratio for the  $\text{Ni}(\text{NO}_3)_2 + \frac{10}{9}\varphi\text{C}_2\text{H}_5\text{NO}_2 + n\text{H}_2\text{O}$  (A) and  $\text{Ni}(\text{NO}_3)_2 + \frac{5}{18}\varphi\text{C}_6\text{H}_{12}\text{N}_4 + n\text{H}_2\text{O}$  (B) gels.

Figure 8: Linear fitting of the  $\ln(V/T_c) - 1/T_c$  plots to extract effective activation energy